PAPER

Check for updates

Combined first-principles calculations and experimental study on the photocatalytic mechanism of natural dolomite

Xiaomin Hou, Qi Cheng, Jianrong Wang, Qingfeng Wu [ID] * and Weibin Zhang [ID] *

Mineral-based photocatalysts have received great attention due to their low cost. In this study, the photocatalytic activity of natural dolomite and its mechanism were investigated based on designed experiments and first-principles calculations. The kinetic study showed that natural dolomite showed notable photocatalytic activity for the degradation of target compounds including methylene blue, diphenhydramine, and tetracycline. The EPR analysis demonstrated that $O_2^{-}\cdot$, $\cdot OH$, and $^1O_2$ were produced in the dolomite system under simulated sunlight irradiation. The first-principles calculations indicated that the isomorphous substitution of Fe^{2+} for Mg^{2+} in the dolomite lattice led to the impurity levels appearing in the forbidden band, which caused a significant decrease of the band gap from 5.02 to 1.63 eV. As a result, natural dolomite could act as a semiconductor photocatalyst in photochemical reactions due to the substitution of Mg^{2+} by Fe^{2+}. Under simulated sunlight irradiation, photogenerated electron–hole pairs in the natural dolomite were separated and transferred to the surface, and then formed reactive radicals through further reactions, thereby enhancing the degradation of target compounds. This research may contribute to the understanding of the photocatalytic activity of natural minerals.

1. Introduction

Natural minerals are widely distributed at the Earth's surface. As important raw materials, they are extensively used in the different branches of industry. In the field of heterogeneous photocatalysis, it has been widely recognized that natural minerals may play an important role as photocatalysts or substrates of photocatalysts due to their low cost.[1–7] So far, a large number of studies have been carried out to investigate the photocatalytic activity of natural minerals, and to further develop mineral-based photocatalytic applications. For example, the photocatalytic activity and mechanisms of natural semiconducting minerals, including rutile,[7,8] iron oxides,[9] sphalerite,[7,10] and manganese oxides,[11] have been widely studied *via* experiments and theoretical calculations, and their applications as photocatalysts in the degradation of toxic and hazardous pollutants are also conducted. A recent study reported the application of natural wolfremite as a novel visible-light photocatalyst for organics degradation.[12] In addition, an excellent review by Lu provides overviews of various natural minerals as potential photocatalysts.[13] Besides semiconductor minerals, several clay minerals such as montmorillonite[14,15] and kaolinite,[16] were demonstrated to have photocatalytic activity

under simulated sunlight irradiation. Moreover, many studies reported that natural minerals were used as substrate materials to synthesize photocatalysts for the enhancement of photocatalytic activity.[17]

A comprehensive understanding of the photocatalytic properties of natural minerals is important to develop mineral-based photocatalytic applications. However, most studies center on natural semiconductor minerals, and few studies focus on the photocatalytic properties of natural carbonate minerals. Dolomite is a double-carbonate mineral with chemical formula $CaMg(CO_3)_2$, and its theoretical compositions consist of 30.41% CaO, 21.86% MgO, and 47.73% CO_2. In natural dolomite, a isomorphous substitution of Mg^{2+} by Fe^{2+} is often observed.[18] As an inexpensive material, dolomite is widely used in different industrial fields, such as building construction, ceramic and plastic production, iron and steel making, soil remediation, and effluent treatment.[19–21] Besides these traditional applications, the dolomite is also applied in the synthesis of composite catalysts. Some studies reported the applications of dolomite based catalyst in the removal of acidic gaseous pollutants and the production of biodiesel and glycerol carbonate.[22,23]

To the best of our knowledge, there is no studies on the photocatalytic properties of natural dolomite. If natural dolomite has photocatalytic activity under sunlight irradiation, it may be used as a novel low-cost photocatalyst, or used to synthesize dolomite-based photocatalyst. Based on this idea, we planned to investigate the photocatalytic properties of natural

School of Physics and Optoelectronic Engineering, Yangtze University, 1 Nanhuan Road, Jingzhou, Hubei 434023, China. E-mail: cjdxwqfscience@163.com; wbzhang@yangtzeu.edu.cn

dolomite, and further discussed its photocatalytic mechanism under sunlight based on the first-principles calculations. This research will contribute to the understanding of the photocatalytic activity and mechanism of natural minerals.

2. Materials and methods

2.1 Materials

The natural dolomite sample used in this work was obtained from Jinyuan Co., Ltd (Zhengzhou, China). Methylene blue (MB), diphenhydramine hydrochloride (DP), and tetracycline hydrochloride (TC) with purity >98% were purchased from Sinopharm Chemical Reagent Co., Ltd (Beijing, China). Chemical reagents including acetonitrile, acetic acid, methanol, and triethylamine were high-performance liquid chromatography (HPLC) grade, and purchased from J&K Chemical Co., Ltd (Beijing, China). The spin-trapping reagents 2,2,6,6-tetramethylpiperidine (TEMP) and 5,5-dimethyl-1-pyrroline N-oxide (DMPO) used for electron paramagnetic resonance (EPR) experiments were supplied by Tokyo Chemical Industry Co., Ltd (Tokyo, Japan). Milli-Q water (18 MΩ cm^{-1}) was used to prepare all solutions.

2.2 Pre-treatment and characterization of the natural dolomite sample

The natural dolomite was first passed through a 100-mesh sieve to obtain a uniform particle size. Then, the obtained sample was cleaned by Milli-Q water for four times, and dried in room temperature for 24 h. No chemical treatments were conducted on the sample in order to preserve its natural attributes. The morphology of the dolomite sample was recorded by a JEOL, JSM-7610F scanning electron microscope (SEM). Powder X-ray diffraction (XRD) pattern was obtained with a Philips X'Pert-Pro diffractometer equipped with Cu-Kα radiation, monitoring in the range from $2\theta = 5$ to $80°$, and the collected data were processed using MDI Jade software (version 6.5). The elemental composition of the dolomite sample was quantified using a S4 Pioneer X-ray fluorescence (XRF) spectrometer (Bruker AXS, Germany). The UV-Vis diffuse reflectance spectra (DRS) of the natural dolomite were measured by a UV-Vis spectrophotometer (U4100, Hitachi) with an integration sphere.

2.3 Photocurrent measurement

The photocurrent measurements were performed on a CHI-660C electrochemistry workstation (Chenhua, China) with a three-electrode system: the dolomite-coated FTO glass (effective area is 1.0 cm^2) as the working electrode, a saturated calomel electrode (SCE) as the reference electrode, and a Pt wire as the counter electrode. The supporting electrolyte was a 0.5 M Na$_2$SO$_4$ aqueous solution. A 150 W xenon light resource with a reflector (300–800 nm) was used as the irradiation source. The photocurrent response was carried out at a constant potential of +0.4 V to the working photoanode. A manual shutter controlled the exposure time of the sample to the light with a interval of 20 s.

2.4 Photoactivity evaluation

Photocatalytic degradation was performed in a PR22-25 photochemical reactor (PerfectLight, China), which is equipped with a PLS-SXE300UV xenon light resource and a DC-0506 water-cooling system (HengPing, Shanghai). The output wavelength range of xenon lamp is in the range between 300 and 800 nm, and the light power input into the reactor was about 120 mW cm^{-2}. During irradiation, the mixture was stirred constantly, and the temperature in the reactor was maintained at 4 °C through circulating water. For each experiment, 0.5 g dolomite sample was dispersed in 100 mL MB (10 mg L^{-1}), DP (20 mg L^{-1}), or TC (20 mg L^{-1}) solution in the 250 mL reactor. And then, the solution containing dolomite was magnetically stirred for 1 h to establish the adsorption equilibrium. At the end of equilibrium, the suspension began to be irradiated. A 2 mL aliquot of the suspension was collected at 15 min intervals, filtered through a 0.22 μm membrane, and analyzed by HPLC or UV-Vis spectrophotometer. All experiments were performed in duplicate for each condition.

2.5 Analytical determination and detection of reactive species

The concentration of MB was measured by a UV-vis spectrophotometer (Shimadzu, UV 2450) at the maximum absorption wavelength of 664 nm. The concentrations of DP and TC were determined with a Shimadzu HPLC (LC-20) equipped with a C18 ODS reversed phase column (4.6 mm × 150 mm, 5 μm) and a SPD20 UV detector. For the determination of DP, the mobile phase consisted of 25 mM acetic acid and acetonitrile (60 : 40, v/v), with pH adjusted to 6.0 ± 0.1 using triethylamine. While for the determination of TC, the mobile phase was composed of 0.01 M oxalic acid, acetonitrile, and methanol (65 : 25 : 15, v/v/v). The detector wavelengths for DP and TC determination were set to 220 and 355 nm, respectively. Isocratic elution was performed at a flow rate 0.8 mL min^{-1}. The injection volume was 20 μL, and oven temperature was kept at 35 °C.

EPR signals of reactive radicals trapped by TEMP and DMPO were detected on a Bruker EMXplus EPR spectrometer equipped with an situ irradiation source (a Quanta-Ray Nd:YAG laser system with $\lambda = 355$ nm). The operating parameters were set as follows: center field 3227.67 G; microwave frequency 9054.62 MHz; power 0.998 mW.
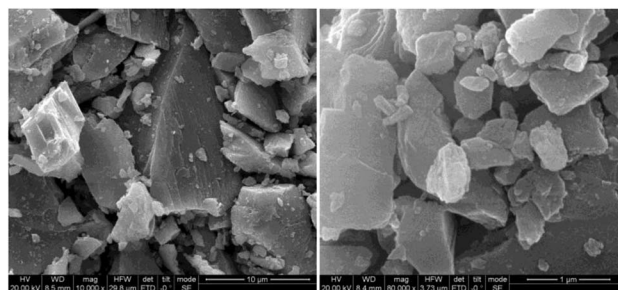

Fig. 1 SEM image of the natural dolomite at different magnifications.
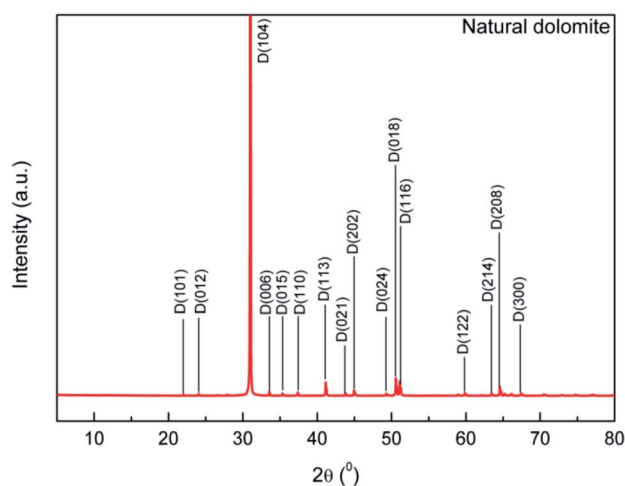
Fig. 2 XRD pattern of the natural dolomite and analysis with MDI Jade 6.5 software.

Table 1 Elemental compositions of natural dolomite determined by X-ray fluorescence spectrometer

Composition (%)								
CO_2	MgO	Al_2O_3	SiO_2	P_2O_5	SO_3	K_2O	CaO	Fe_2O_3
52.6	23.8	0.153	0.135	0.008	0.048	0.014	21.4	1.84

2.6 Method of calculation

To probe the photocatalytic mechanism of natural dolomite, the first-principles calculations based on the density functional theory (DFT) were carried out using the Vienna *Ab initio* Simulation Package (VASP).[24] The generalized gradient approximation (GGA) with the Perdew–Burke–Ernzerhof (PBE) parametrization were employed to deal with the exchange–correlation functional.[25,26] The energy cutoff for plane-wave basis was set at 500 eV, and a $4 \times 4 \times 1$ Monkhorst–Pack k-point mesh was used for the Brillouin zone integration.[27,28] For each calculation, the convergence thresholds for the maximum energy change and force were 1.0×10^{-5} eV per atom and 0.01 eV $Å^{-1}$ per atom, respectively. As shown in Fig. 7(a), a $2 \times 2 \times 1$ supercell

(including 6 C, 18 O, 3 Mg, and 3 Ca atoms) was built to model the natural dolomite, and the lattice parameters of unit cell were $a = b = 4.81$ Å, $c = 16.01$ Å.[29] To simulate the isomorphous substitution of Fe^{2+} for Mg^{2+} in natural dolomite, the Mg^{2+} ions in the unit cell are randomly replaced by Fe^{2+} ions, with the number of Fe^{2+} ions varying from 1 to 9. The random substitution of 3 Fe^{2+} for 3 Mg^{2+} in the unit cell is shown in Fig. 7(b).

3. Results and discussion

3.1 Characterization results

SEM images of the natural dolomite are depicted in Fig. 1, which indicated a smooth surface morphology, characteristic of dolomite. Such a microstructure was attributed to the deposition environment of carbonates, and generally led to low internal porosity and surface area.

The XRD pattern of the sample showed that characteristic reflections of dolomite (Fig. 2). Main peaks of the dolomite sample located at 31.0, 33.5, 37.3, 41.1, 44.9, and 50.5°, which was consistent with that reported by Sdiri.[30] No obvious peaks of impurities was observed, indicative of a high purity dolomite.

Chemical compositions of the dolomite sample determined by XRF analysis showed high amounts of CaO and MgO (Table 1), indicating a high purity dolomite. Besides, the dolomite sample also contained a small amount of impurities, such as SiO_2, Al_2O_3, and Fe_2O_3. Among of them, the content of Fe_2O_3 reached 1.84%, which could be ascribed to the isomorphous substitution of Mg^{2+} by Fe^{2+} in the dolomite lattice.

The UV-vis DRS spectra of the sample is shown in Fig. 3. It indicated that the natural dolomite exhibited significant absorption in the wavelength range of 200–600 nm, with a absorption maximum at 228 nm (Fig. 3(a)). Based on this spectra, the energy band gap of the natural dolomite obtained from extrapolation of linear portion of the absorption edge was estimated to be 1.28 eV,[31] suggesting a semiconducting nature (Fig. 3(b)).

3.2 Photocatalytic degradation of MB, DP and TC by natural dolomite

To examine the photocatalytic activity of natural dolomite, the MB, DP, and TC were selected as target compounds to model
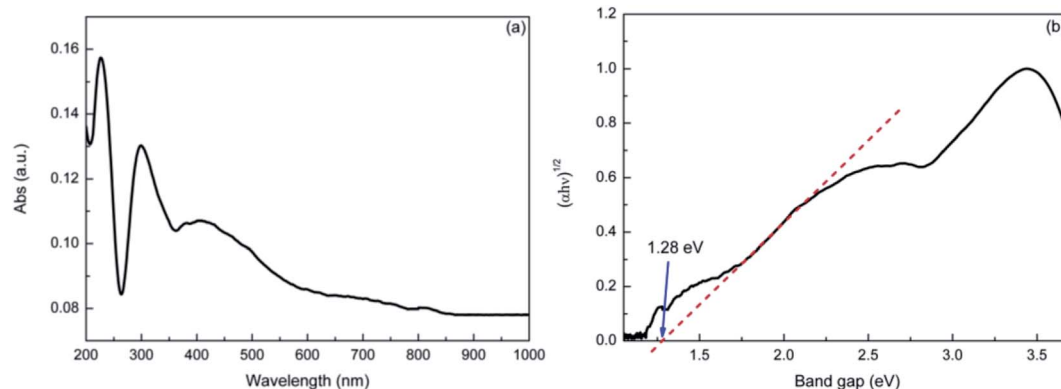

Fig. 3 The UV-Vis diffuse reflectance spectra of natural dolomite (a), and the estimated band gap (b).

organic pollutants. MB is a dye, a compound widely used in evaluating the catalytic performance of photocatalyst. DP and TC are two pharmaceuticals, which belong to emerging pollutants. Fig. 4 displays the photodegradation of MB, DP, and TC *versus* irradiation time in the absence and presence of natural dolomite, as well as the dark controls with dolomite. The degradation rates for MB, DP, and TC in pure aqueous phase were 53%, 12%, and 7%, respectively, and the photolysis kinetics obeyed the pseudo-first order kinetics, with rate constants 0.46×10^{-2}, 0.16×10^{-2}, and 0.09×10^{-2} min^{-1} (Table 2). When the natural dolomite was added to the solution, the degradation rates for MB, DP and TC increased to 79%, 62% and 80%, respectively, with the corresponding rate constants increased to 0.87×10^{-2}, 1.29×10^{-2}, and 2.13×10^{-2} min^{-1} (Table 2). The dark controls were performed to determine the adsorption of target compounds on the dolomite during irradiation. The results showed that the loss of MB, DP, and TC caused by adsorption were about 11%, 5%, and 9%, respectively. Apparently, the degradation rates calculated after deducting the amount of adsorption significantly increased in the presence of natural dolomite. This result suggested that the natural dolomite had notable photocatalytic activity, and could be use as a potential photocatalyst. In addition, from an environmental perspective, the natural dolomite may also play an important role in environmental self-purification.

Table 2 Fitted parameters for MB, DP, and TC photodegradation in the absence and presence of natural dolomite by pseudo-first-order model

Reaction condition	K_{DP} (min^{-1})	R^2
MB in water	$(0.46 \pm 0.02) \times 10^{-2}$	0.994
MB + dolomite	$(0.87 \pm 0.07) \times 10^{-2}$	0.967
DP in water	$(0.16 \pm 0.02) \times 10^{-2}$	0.998
DP + dolomite	$(1.29 \pm 0.08) \times 10^{-2}$	0.982
TC in water	$(0.091 \pm 0.004) \times 10^{-2}$	0.991
TC + dolomite	$(2.13 \pm 0.08) \times 10^{-2}$	0.993

In order to evaluate the recyclability and stability of the natural dolomite in the photocatalytic applications, cycling experiments were performed. The results illustrated that the degradation rate for DP, MB, and TC was 62%, 78%, and 79% in the first cycle, respectively, but significantly decreased to 30%, 46%, and 66% in the second cycle (Fig. 5). At the end of 3 cycles, the photocatalytic activity of the natural dolomite further decreased, suggesting that deactivation of the dolomite could occurred after repeated applications.

3.3 Detection of reactive oxygen species

Usually, photogenerated reactive oxygen species (ROS), including hydroxyl radical ($^{\bullet}$OH), superoxide anion radical
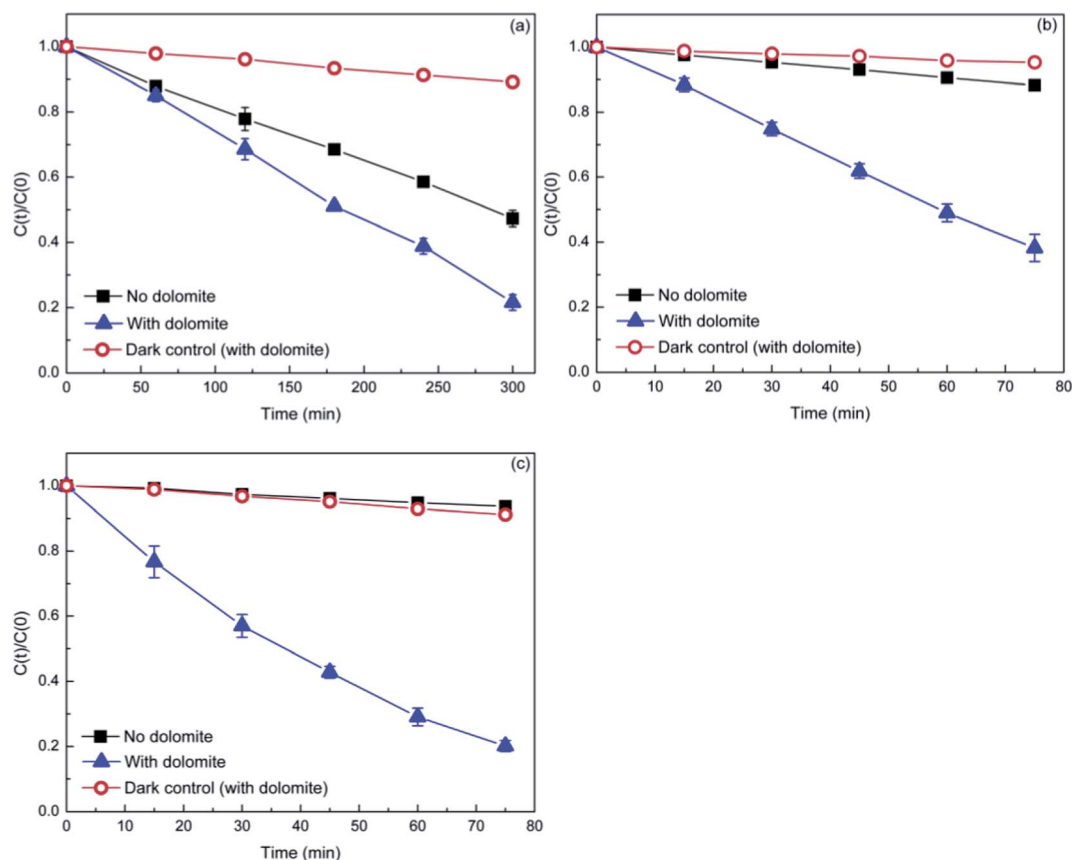

Fig. 4 Photocatalytic degradation of MB (a), DP (b), and TC (c) in the presence of the natural dolomite (0.5 g). The initial concentrations of MB, DP, and TC are 10, 20, and 20 mg L^{-1}, respectively.
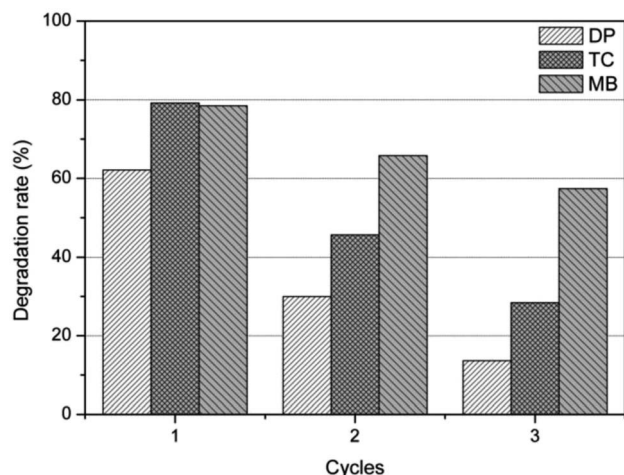
Fig. 5 Photocatalytic activity of the natural dolomite after repeated use for 3 times.

$(O_2{}^{-\cdot})$, and singlet oxygen ($^1O_2$) are often considered to play a crucial role in photocatalytic reactions. Therefore, it is reasonable to speculate that the enhanced degradation of target compounds may also be attributed to the photogenerated ROS in the dolomite system. As such, the EPR spin-trapping experiments was performed to determine the ROS produced in the irradiated dolomite system. As shown in Fig. 6, no obvious signal was detected in the dark condition, but after irradiation, the characteristic peaks of TEMP–$^1O_2$, DMPO–$O_2{}^{-\cdot}$, and DMPO–OH adducts appeared, and gradually strengthened with the irradiation time. This result clearly demonstrated the generation of $^1O_2$, $O_2{}^{-\cdot}$, and $\cdot$OH in the dolomite system under simulated sunlight irradiation. Furthermore, the strong signals indicated that the radicals generated in the dolomite system was considerable. These reactive radicals further reacted with target compounds, resulting in their enhanced degradation.

3.4 Photocatalytic mechanisms of the natural dolomite

Density functional theory calculations were performed to further probe the photocatalytic mechanism. Fig. 8 displays the electronic band structure of pristine and Fe^{2+}-substituted dolomite. For the pristine dolomite, the band gap energy is calculated to be 5.02 eV (Fig. 8(a)), which is consistent with the result previously reported by Hossain *et al.*[32] With the substitution of 3 Mg^{2+} ions by 3 Fe^{2+} ions, there are two impurity levels appearing in the forbidden band, causing the maximum band gap to be reduced to 2.04 eV (Fig. 8(b)). As more Mg^{2+} are substituted by Fe^{2+} ions, more impurity levels arise in the forbidden band, and the impurity bands widen, thereby causing
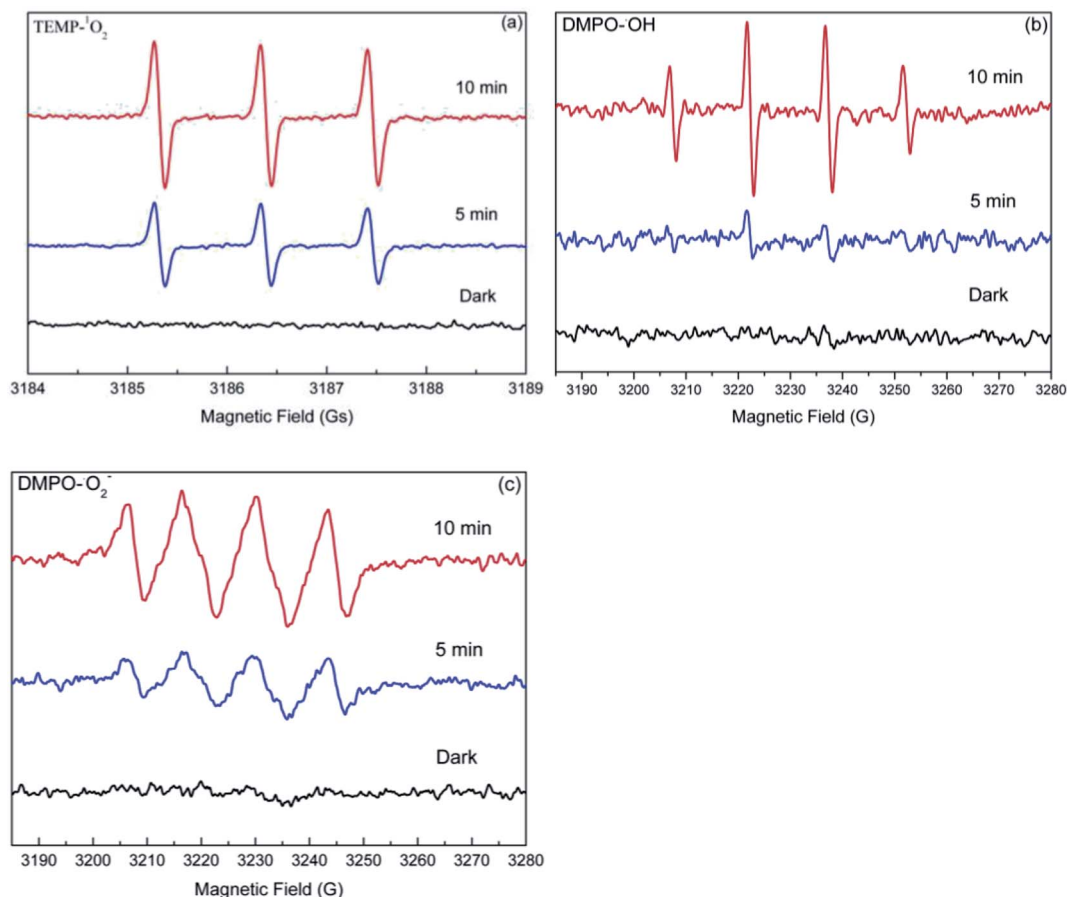

Fig. 6 EPR spectra of the TEMP–$^1O_2$ (a), DMPO–$\cdot$OH (b), and DMPO–$O_2{}^{-\cdot}$ (c) adducts generated in the natural dolomite system after simulated sunlight irradiation.
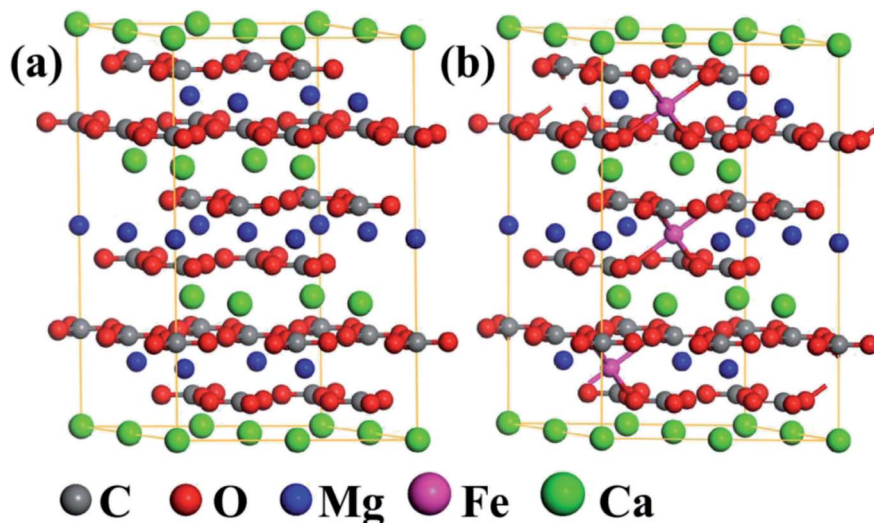
Fig. 7   The optimized structures of (a) the $2 \times 2 \times 1$ dolomite supercell, and (b) the supercell with substitution of 3 Fe^{2+} for 3 Mg^{2+}.

a further decrease of the band gap. When 9 Mg^{2+} ions are replaced, the maximum band gap decreases to 1.63 eV (Fig. 8(d)), which is close to the band gap (1.28 eV) estimated from the UV-Vis reflectance spectra of the natural dolomite (Fig. 3(b)). The decrease of band gap from 5.02 to 1.63 eV

suggests that the natural dolomite could exhibit the characteristics of a semiconductor photocatalyst after partial substitution of Mg^{2+} by Fe^{2+}.

Densities of states (DOS) for pristine and Fe^{2+}-substituted dolomite is presented in Fig. 9. According to the DOS, the
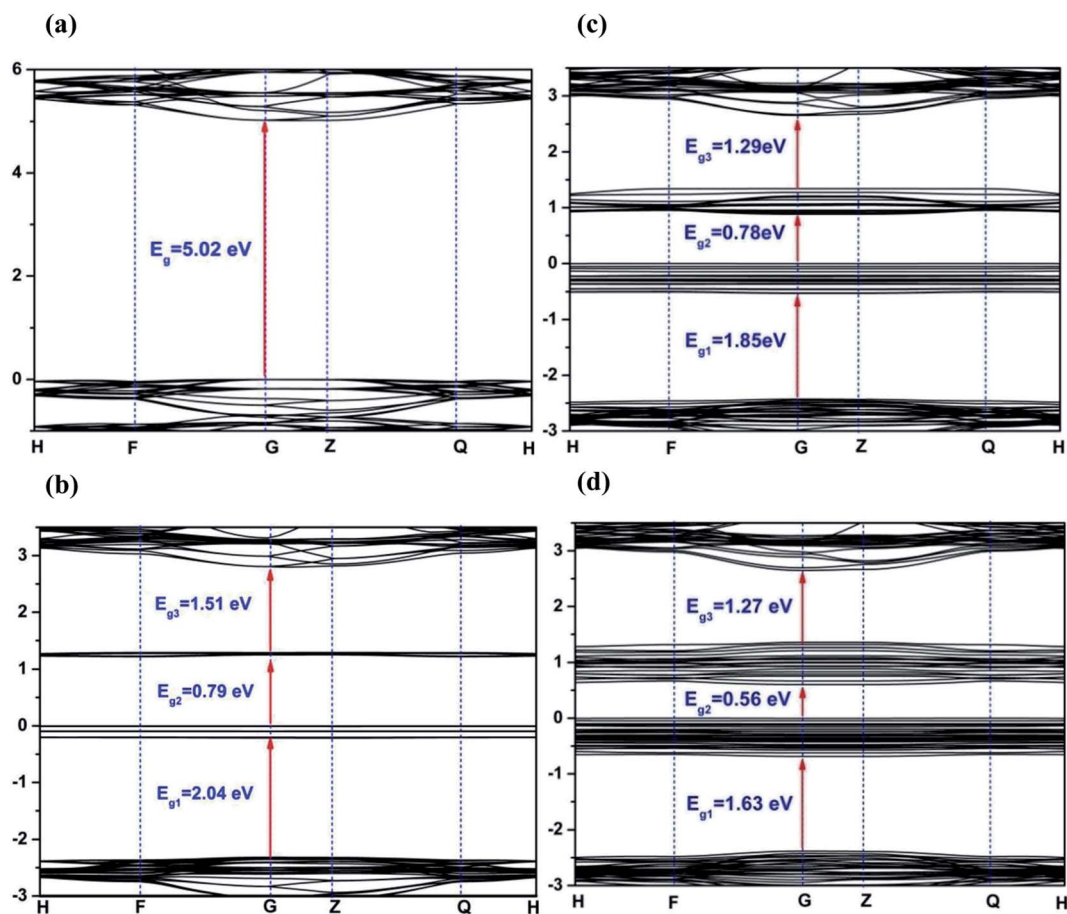

Fig. 8   Band structures of dolomite supercell with 0 (a), 3 (b), 6 (c), and 9 (d) Fe^{2+} substitution. The Fermi level is set to 0.
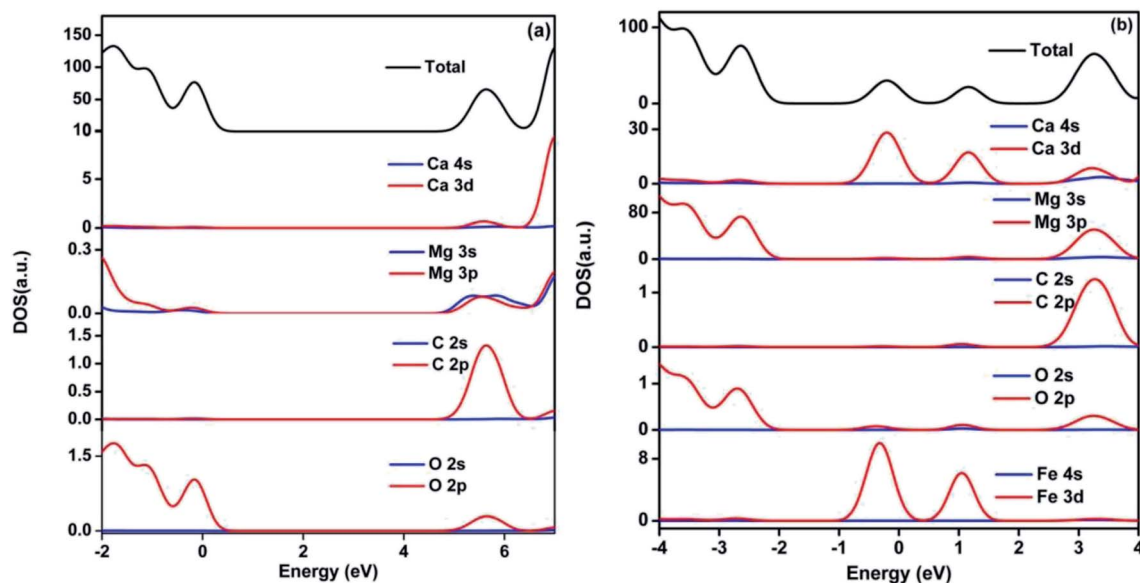
Fig. 9 Density of state of pristine (a) and 3 Fe^{2+}-substituted (b) dolomite. The Fermi level is set to 0.

valence band is mainly composed of O 2p state, and the conduction band consists of O 2p, C 2p, Mg 3p, and Ca 3d states, but the role of C 2p state is major (Fig. 9(a)). The two impurity bands appearing in the forbidden gap are predominantly contributed by Fe 3d and Ca 3d states (Fig. 9(b)), and show more delocalization with the increasing concentration of Fe^{2+}.

In summary, the results obtained from theoretical calculations demonstrated that the substitution of Fe^{2+} for Mg^{2+} in the dolomite lattice resulted in the decrease of band gap, which caused the natural dolomite to exhibit photocatalytic activity. To further verify the photocatalytic mechanism, photocurrent was measured for the natural dolomite (Fig. 10). It was clear that obvious photocurrent response were observed, indicating a photoinduced electrons and holes separation.
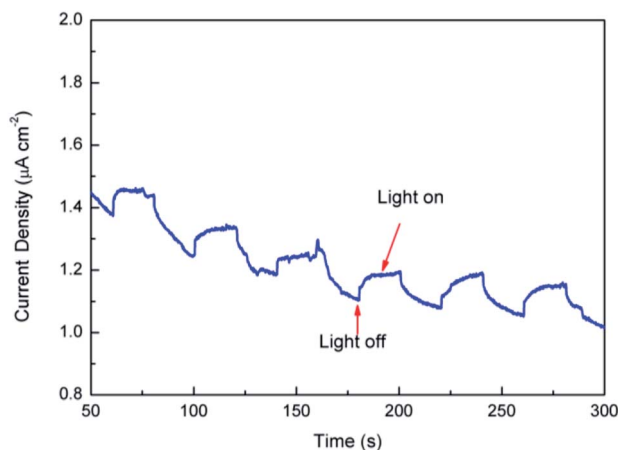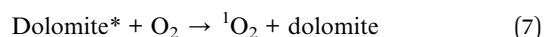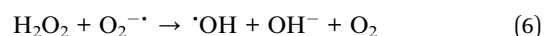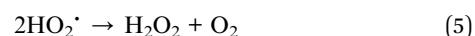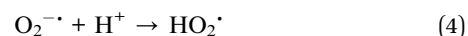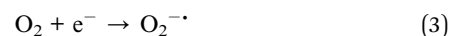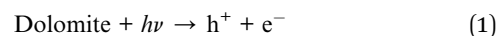

Fig. 10 Photocurrent of the natural dolomite under simulated sunlight irradiation.

On the basis of the above results, the photocatalytic mechanism for the natural dolomite was proposed. Under simulated sunlight irradiation, photoinduced electrons and holes separate and migrate to the dolomite surface (eqn (1)). Then, further reactions according to eqn (2)–(6) led to the formation of $^{\cdot}OH$ and $O_2^{-\cdot}$. As to the generation of $^1O_2$, it might be ascribed to the energy transfer between excited dolomite and dissolved oxygen in aqueous solution (eqn (7)).

$$\text{Dolomite} + h\nu \rightarrow h^+ + e^- \tag{1}$$

$$H_2O + h^+ \rightarrow {}^{\cdot}OH + H^+ \tag{2}$$

$$O_2 + e^- \rightarrow O_2^{-\cdot} \tag{3}$$

$$O_2^{-\cdot} + H^+ \rightarrow HO_2^{\cdot} \tag{4}$$

$$2HO_2^{\cdot} \rightarrow H_2O_2 + O_2 \tag{5}$$

$$H_2O_2 + O_2^{-\cdot} \rightarrow {}^{\cdot}OH + OH^- + O_2 \tag{6}$$

$$\text{Dolomite*} + O_2 \rightarrow {}^1O_2 + \text{dolomite} \tag{7}$$

Besides, considering the release of trace Fe ions into the solution during irradiation, it could be speculated that the photo-Fenton-like reaction induced by released Fe ions might also contribute to the degradation of target compounds.

4. Conclusion

For the first time, the photocatalytic activity of natural dolomite was investigated using MB, DP, and TC as target compounds, and the mechanism was further discussed based on EPR analysis and the first-principles calculations. The results indicated that the natural dolomite had notable photocatalytic activity for the degradation of the target compounds. The EPR analysis

demonstrated that $^1O_2$, $O_2^{-\cdot}$, and $\cdot OH$ generated in the irradiated dolomite system, and are responsible for the accelerated degradation of target compounds. The first-principles calculations indicated that the partial substitution of Fe^{2+} for Mg^{2+} in the dolomite lattice led to the impurity bands appearing in the forbidden gap, causing a significant decrease of band gap. Therefore, the natural dolomite could exhibit the properties of semiconductor photocatalyst in photoreactions. Based on these results, the mechanism of natural dolomite photocatalysis was proposed. First, the dolomite excited by simulated sunlight generates electrons and holes, which subsequently migrate to the dolomite surface, and react to form ROS *via* further reactions. Second, the ROS react with target compounds to cause their degradation.

Conflicts of interest

There are no conflicts to declare.

Acknowledgements

References

1 D. Papoulis, *Appl. Clay Sci.*, 2019, **168**, 164–174.

2 B. Szczepanik, *Appl. Clay Sci.*, 2017, **141**, 227–239.

3 Y. Zhang, H. Gan and G. Zhang, *Chem. Eng. J.*, 2011, **172**, 936–943.

4 O. Kozák, P. Praus, K. Kočí and M. Klementová, *J. Colloid Interface Sci.*, 2010, **352**, 244–251.

5 T. Liu, X. Chen, Y. Dai, L. Zhou, J. Guo and S. Ai, *J. Alloys Compd.*, 2015, **649**, 244–253.

6 Y. Li, C. Ding, Y. Liu, Y. Li, A. Lu, C. Wang, and H. Ding, Visible light photocatalysis of natural semiconducting minerals, in *Advances in Photocatalytic Disinfection. Green Chemistry and Sustainable Technology*, ed. T An, T Zhao, and P Wong, Springer, Berlin, Heidelberg, 2017.

7 M. A. A. Schoonen, Y. Xu and D. R. Strongin, *J. Geochem. Explor.*, 1998, **62**, 201–215.

8 R. I. Bickley, G. Munuera and F. S. Stone, *J. Catal.*, 1973, **31**, 398–407.

9 S. Belaidi, N. Setifi, L. Mammeri, W. Remache, K. Benhamouda, T. Sehili and K. Djebbar, *Desalin. Water Treat.*, 2018, **113**, 171–178.

10 Y. Li, A. Lu and C. Wang, *Acta Geol. Sin. (Engl. Ed.)*, 2009, **3**, 633–639.

11 S. Ristig, N. Cibura and J. Strunk, *Green*, 2015, **5**, 1–6.

12 L. Li, Y. Li, Y. Li, A. Lu, H. Ding, P. K. Wong, H. Sun and J. Shi, *Catal. Today*, 2019, **358**, 177–183.

13 A. Lu, *Acta Petrol. Mineral.*, 2003, **22**, 323–331.

14 Y. Liu, X. Zhang and F. Wu, *Appl. Clay Sci.*, 2010, **49**, 182–186.

15 Q. Wu, Z. Que, Z. Li, S. Chen, W. Zhang, K. Yin and H. Hong, *J. Hazard. Mater.*, 2018, **359**, 414–420.

16 D. Kibanova, M. Trejo, H. Destaillats and J. Cervini-Silva, *Catal. Commun.*, 2011, **12**, 698–702.

17 H. Van Damme, F. Bergaya, and D. Challal, Photocatalysis over clay supports, in *Homogeneous and heterogeneous photocatalysis*, ed. E. Pelizzetti and N. Serpone, Springer, Dordrecht, 1986.

18 R. J. Reeder and W. A. Dollase, *Am. Mineral.*, 1989, **74**, 1159–1167.

19 O. Sivrikaya, *Ironmaking Steelmaking*, 2018, **45**, 764–772.

20 R. Marouf, N. Khelifa, K. Marouf-Khelifa, J. Schott and A. Khelifa, *J. Colloid Interface Sci.*, 2006, **297**, 45–53.

21 M. Shaaban, Q. Peng, S. Lin, Y. Wu, M. S. Khalid, L. Wu, Y. Mo and R. Hu, *Catena*, 2016, **140**, 9–14.

22 L. M. Correia, N. D. S. Campelo, D. S. Novaes, C. L. Cavalcante, J. A. Cecilia, C. E. Rodríguez and R. S. Vieira, *Chem. Eng. J.*, 2015, **269**, 35–43.

23 Y. T. Algoufi, G. Kabir and B. H. Hameed, *J. Taiwan Inst. Chem. Eng.*, 2017, **70**, 179–187.

24 G. Kresse and J. Furthmüller, *Comput. Mater. Sci.*, 1996, **6**, 15–50.

25 B. Hammer, L. B. Hansen and J. K. Norskov, *Phys. Rev. B: Condens. Matter Mater. Phys.*, 1999, **59**, 7413–7421.

26 W. Zhang and Y. Xiao, *Energy Fuels*, 2020, **34**, 2425–2434.

27 Q. Wang, Z. Q. Liu, D. M. Liu, W. Wang, Z. W. Zhao, F. Y. Cui and G. B. Li, *Chem. Eng. J.*, 2019, **360**, 838–847.

28 W. Zhang and Y. Xiao, *Energy Fuels*, 2020, **34**, 2425–2434.

29 J. Warren, *Earth-Sci. Rev.*, 2000, **52**, 1–81.

30 A. Sdiri, *Environ. Prog. Sustainable Energy*, 2018, **37**, 1–8.

31 Y. Xu, W. Wen and J.-M. Wu, *J. Hazard. Mater.*, 2018, **343**, 285–297.

32 F. M. Hossain, G. E. Murch, I. V. Belova and B. D. Turner, *Solid State Commun.*, 2009, **149**, 1201–1203.